

Article

Development of an Aluminum-Based Hybrid Billet Material for the Process-Integrated Foaming of Hollow Co-Extrusions

Florian Patrick Schäfke ^{*}, Susanne Elisabeth Thürer , Hans Jürgen Maier  and Christian Klose 

Institut für Werkstoffkunde (Materials Science), Leibniz University Hannover, An der Universität 2, 30823 Garbsen, Germany; thuerer@iw.uni-hannover.de (S.E.T.); maier@iw.uni-hannover.de (H.J.M.); klose@iw.uni-hannover.de (C.K.)

* Correspondence: schaeffe@iw.uni-hannover.de; Tel.: +49-511-762-4314

Abstract: Metal foams are attractive for lightweight construction in the automotive sector since they provide high-energy absorption and good damping properties, which is crucial, e.g., for crash structures. Currently, however, foams are produced separately and then pasted into the components. Consequently, the overall mechanical properties depend significantly on the quality of the adhesive bond between the foam and the structural component. A new process route for the manufacture of hybrid foamed hollow aluminum profiles is proposed. In this approach, a foamable precursor material is directly integrated into the extrusion process of the hollow structural profile. To this end, special low-melting alloys were developed in this study to enable foaming inside the aluminum profile. The melting intervals of these alloys were examined using differential scanning calorimetry. One of the promising AlZnSi alloys was atomized, mixed with a foaming agent and then compacted into semi-finished products for subsequent co-extrusion. The foaming behavior, which was investigated by means of X-ray microscopy, is shown to depend primarily on the mass fraction of the foaming agent as well as the heat treatment parameters. The results demonstrate that both the melting interval and the foaming behavior of AlZn22Si6 make this particular alloy a suitable candidate for the desired process chain.

Keywords: metal foam; process-integrated foaming; extruded aluminum profiles; X-ray microscopy



Citation: Schäfke, F.P.; Thürer, S.E.; Maier, H.J.; Klose, C. Development of an Aluminum-Based Hybrid Billet Material for the Process-Integrated Foaming of Hollow Co-Extrusions. *Metals* **2021**, *11*, 1382. <https://doi.org/10.3390/met11091382>

Academic Editor: Jeff Th. M. De Hosson

Received: 4 August 2021

Accepted: 25 August 2021

Published: 31 August 2021

Publisher's Note: MDPI stays neutral with regard to jurisdictional claims in published maps and institutional affiliations.



Copyright: © 2021 by the authors. Licensee MDPI, Basel, Switzerland. This article is an open access article distributed under the terms and conditions of the Creative Commons Attribution (CC BY) license (<https://creativecommons.org/licenses/by/4.0/>).

1. Introduction

Cellular metals such as light alloy foams can offer both a higher specific strength and stiffness as well as higher energy absorption and damping capacity compared to compact solid materials of the same alloy. These properties are crucial for an application in lightweight construction, e.g., in the automotive and transportation industry. Early practical examples are engine mounts made of aluminum foam sandwich (AFS) manufactured by the automotive company Wilhelm Karmann GmbH. In this case, an outer support structure is joined with the previously produced metal foam in a separate joining process to achieve weight reduction while increasing the bending and torsional stiffness and absorbing kinetic energy [1,2]. Various process routes are available to produce cellular materials, resulting in either open-pored or closed-pored foam structures. The latter are mainly produced using the powder metallurgical process route: A metal powder is mixed with a blowing agent, usually a metal hydride powder, and compacted into a semi-finished product. Subsequently, heat treatment leads to the decomposition of the blowing agent, which releases the gas needed for the foaming process. Simultaneously, the metal alloy must reach its melting interval to ensure that the cellular structure is formed [1–5]. Aluminum hollow sections produced by extrusion are increasingly used in the transport industry due to their lightweight properties, which have a positive effect on CO₂ emissions or even the consumption of energy. The focus is on energy absorption and the maximum bending load for crash related components. On the one hand, it was shown that the extrusion process can increase the yield strength and tensile strength of aluminum profiles as a

result of grain refinement [6]. Furthermore, it was shown that the die geometry, especially the material flow controlling geometry elements such as chamfers and radii, has a great influence on the microstructure and the straightness of the hollow sections [7]. On the other, by inserting metal foams into extruded hollow sections in order to manufacture so-called foam-filled tubes (FFT), the maximum bending load and energy absorption capacity can be increased [1,3,8,9]. For instance, the bending load of welded steel tubes was reported to be increased by a factor of three by local reinforcement using magnesium foams [10]. A process that separates the two main steps, i.e., foam production and part shaping, in order to achieve slightly higher flexibility is Advanced Pore Morphology (APM) technology. Here, small-volume foam elements, which were previously produced and fully foamed, are joined together to form a larger element, which is then used to manufacture pure foam parts, foam-filled hybrid structures and sandwich structures with a cellular core layer [11,12]. In addition to an adhesive bond, which strongly influences the mechanical properties of the composite [13], this method has another specific characteristic. The following two types of porosity result from the fact that smaller APM foam elements are first foamed independently, then bonded together to form a larger structure and subsequently glued into a hollow structural profile:

- inner porosity of each APM foam element;
- outer porosity of an assembly of many APM foam elements, which varies with different APM foam element sizes [14].

In another method described as *ex situ* FFT by Duarte et al., a metal foam is created, adapted to the internal dimensions of a thin-walled tube by machining and then inserted into the tube. This creates an air gap between the foam core and the tube, which has a negative effect on the load transfer between the tube and the core elements, and thus the overall mechanical properties of the structure [8].

In order to avoid the disadvantages of the methods described above, a new process chain for the manufacture of foam-filled tubes by employing the process-integrated expansion of a low-melting, foamable precursor material has been developed in the present study. As a result, gluing processes are no longer necessary since air gaps between the foam core and the tube are avoided due to the creation of a metallurgical bond between the foam and the extrusion. The energy required for the process chain-integrated foaming of extruded profiles is provided, on the one hand, by the forming energy that leads to a temperature increase inside the forming zone [15], which strongly depends on the extrusion ratio. On the other hand, full foaming of the hollow cavity of the extrusions is achieved by the heat treatment that is mandatory for hardenable aluminum alloys such as 6000 series wrought alloys that are typically used in lightweight construction, since these require a T6 treatment to achieve their nominal mechanical properties [16].

The hybrid profile investigated in this study, therefore, consists of the following two components: an outer structural element made of the alloy EN AW-6082 (AlSi1MgMn, abbreviated 6082) and the internal foam structure, whose expansion is triggered by the temperature increase resulting from forming and by additional heat from the subsequent T6 heat treatment. Figure 1 shows the developed process chain schematically. A low-melting aluminum alloy (in powder form) is used as the foamable precursor and mixed with a foaming agent. Both are then compacted into a billet, which is formed into a hollow profile together with the support structure by co-extrusion. This process step corresponds to a co-extrusion process using modified billets [17]. In a second step, hybrid billets and a custom toolset featuring a fixed mandrel setup are employed to establish the parameters for the co-extrusion process that is used to produce the final hybrid hollow profiles containing the foam and, thus, complete the envisaged manufacturing route. The current study addresses the area highlighted in red in Figure 1, i.e., it focuses on the necessary initial alloy development process and production of a suitable foamable semi-finished product.

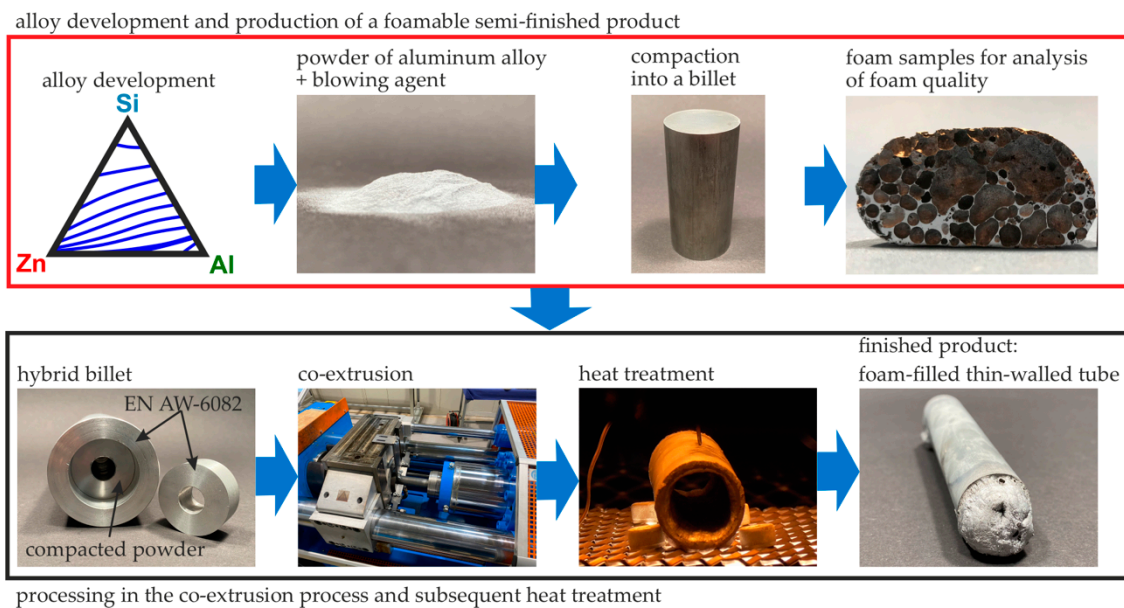


Figure 1. Illustration of the developed process chain for the production of FFTs with a metallurgical bond between foam and the outer wall of the tube; highlighted in the red box are the contents of the present study.

2. Materials and Methods

In this study, eight Al-Zn-Si alloys with compositions along the eutectic channel were produced by casting, cf. Section 2.3. The melting intervals as well as foaming properties were investigated in order to determine suitable alloy compositions with a fitting melting interval for the intended process route. The most promising candidate material was then atomized using an Electrode Induction-melting Gas Atomization (EIGA) process. The powder was blended with the blowing agent (TiH_2) and the mixture was then compacted into foamable semi-finished products for use in a co-extrusion process.

2.1. Determination of the Appropriate Melting Temperature Interval

In order to be able to start the expansion process of the foamable precursor during co-extrusion, the effective temperature increase caused mainly by internal friction of the formed alloy inside the forming zone of the die had to be determined. For this purpose, reference extrusion experiments were performed using conventional billets of the alloy EN AW-6082. A toolset that had two types of mandrels to enable the production of hollow profiles with two different wall thicknesses was used. The mandrel parts that define the inner diameter of the profile ($\varnothing_{\text{inner}}$), had a diameter of either 12 or 16 mm. The die defines the outer diameter of the profile ($\varnothing_{\text{outer}}$). Its diameter was 20 mm in each case to ensure that tubes with a wall thickness of either 4 or 2 mm could be produced with these tools. Billets, each with an outer diameter of 55 mm as well as a central bore fitting the respective mandrel, were used. This resulted in extrusion ratios of 13:1 and 22:1, respectively. By placing the tip of a thermocouple type K near the bearing surface of the die (see Figure 2), the increase in temperature due to forming was recorded in close proximity to the forming zone. The billet, container and die were preheated to 450 °C and a ram speed of 2 mm/s was chosen. All extrusion experiments were performed on a laboratory extrusion press (mueller engineering, Todtenweis, Germany) with a maximum ram force of 2.5 MN. The temperature data resulting from these preliminary investigations were then used to define the target melting temperature range of the foamable material.

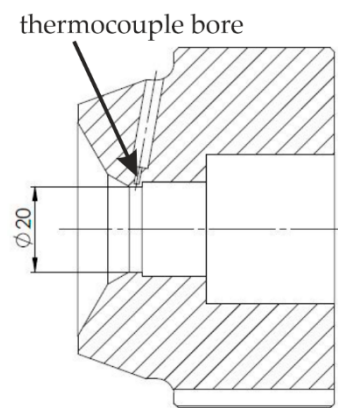


Figure 2. Sectional view of the die with thermocouple bore.

2.2. Alloy Development

It is known that the addition of zinc and silicon results in a decrease in the liquidus temperature of aluminum, and thus both elements were used for the development of a tailored low-melting aluminum alloy [18–20]. The liquidus temperatures of the ternary aluminum–zinc–silicon alloy system are shown in Figure 3 based on thermodynamic calculations by Suzuki [21]. The liquidus temperatures along the eutectic channel (highlighted with a bold blue line in Figure 3) rise from 381 °C on the zinc-rich side to 557 °C on the silicon-rich side. For the investigations in this study, eight promising alloy compositions along the eutectic channel were selected, see detail in Figure 3.

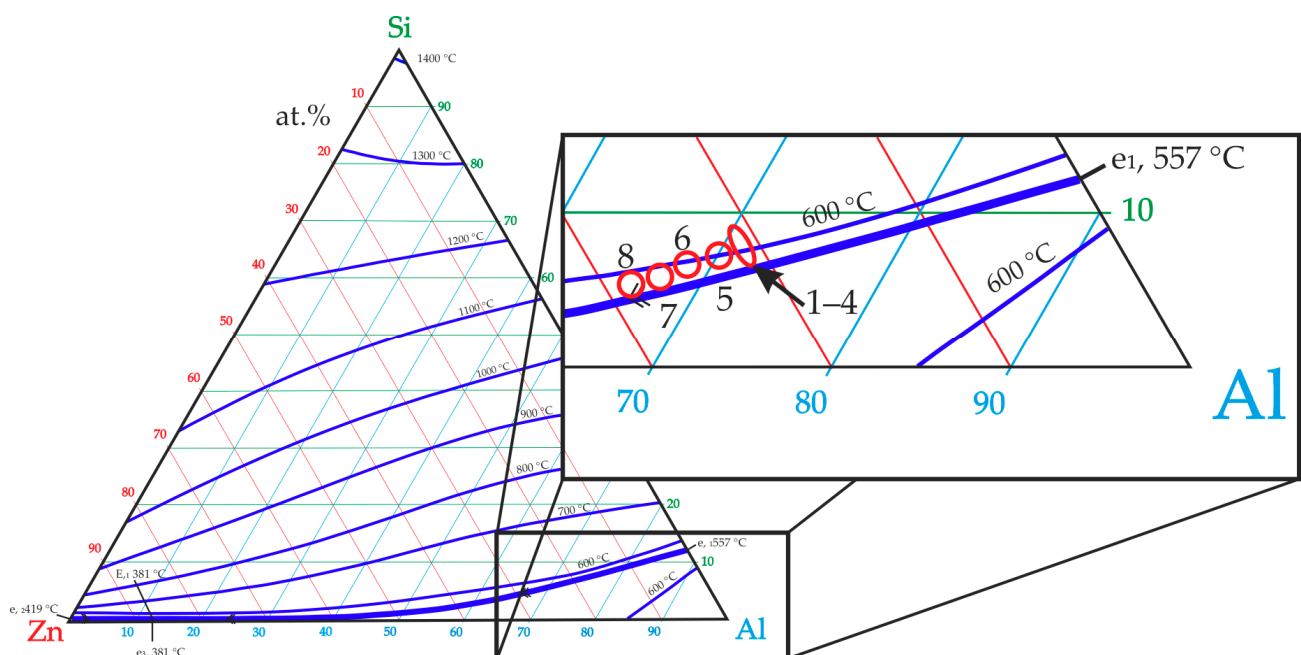


Figure 3. Liquidus plot of the aluminum–zinc–silicon phase diagram according to [21] with the selected alloy compositions 1–8 highlighted by red symbols.

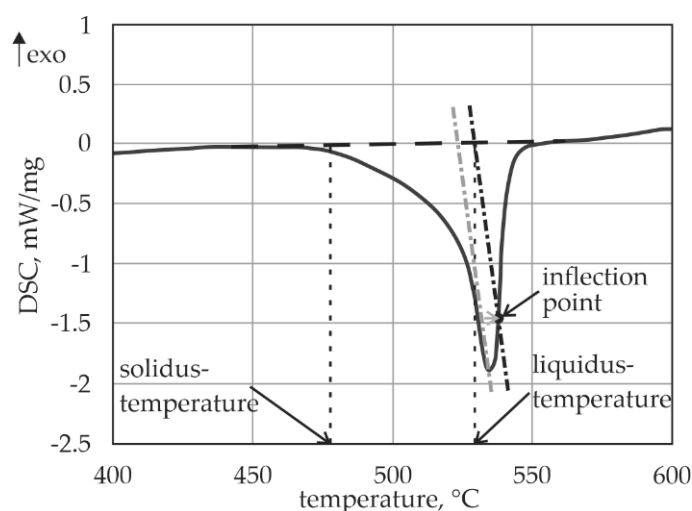
For the aluminum alloys 1–4, the zinc content was kept constant at 22.0 at.%. To study the influence of silicon on the properties of the foamable alloy, the silicon content was varied between 6.0 and 8.0 at.%. Additional compositions with higher zinc contents (alloy 5–8) were investigated in order to probe a possible further reduction in the melting temperatures. The target compositions of the selected alloys are shown in Table 1.

Table 1. Designation and nominal compositions of the low-melting aluminum alloys in at. %.

Alloy No.	Designation	Zn Content (Nominal)	Si Content (Nominal)	Al Content
1	Al-Zn22-Si6	22.0	6.0	balance
2	Al-Zn22-Si6.5	22.0	6.5	balance
3	Al-Zn22-Si7.5	22.0	7.5	balance
4	Al-Zn22-Si8	22.0	8.0	balance
5	Al-Zn23.5-Si8.5	23.5	8.5	balance
6	Al-Zn25-Si7.0	25.0	7.0	balance
7	Al-Zn26-Si6.5	26.0	6.5	balance
8	Al-Zn28-Si5	28.0	5.0	balance

2.3. Casting Process of the Selected Alloys

The eight different low-melting alloys were produced by gravity die-casting. A laboratory-scale tilting crucible furnace with inert gas atmosphere (Argon 5.0) was used for this purpose. The individual components were weighed relative to the target composition shown in Table 1, heated at 680 °C for 60 min inside a cp-titanium crucible and then mechanically stirred for 10 min with a cp-titanium stirrer. Both the crucible and the stirrer were coated with boron nitride prior to the experiments. In order to determine the most promising low-melting alloy for the planned process route (Figure 1), their melting intervals were determined by differential scanning calorimetry (DSC) using an STA 449 C instrument (Erich Netzsch GmbH & Co. Holding KG; Selb, Germany). The DSC measurements were performed at a heating rate of 10 K/min in the temperature range from 30 to 750 °C. The heating curve of the alloys was used to determine the melting interval, as shown in Figure 4. The beginning of the melting interval could be determined directly from the change in the slope of the heating curve in the DSC diagram. To compensate for the heat inertia of the measurement device (changes in thermal conductivity with time, heat inertia of the sensor system), the end of the melting interval was calculated. For this purpose, the baseline was interpolated for a course without exothermal or endothermal reaction in the sample. To interpret the DSC diagrams, a tangent was applied to the approximately linear part of the curve after the point of steepest slope and then shifted to the inflection point of the heating curve after the maximum. The intersection of this tangent with the interpolated baseline indicates the end of the melting interval. This procedure was chosen to compensate for the change in heat conduction with time in the system and to include the inertia of the sensors [22].

**Figure 4.** Principle of evaluating the heating curves of the DSC measurements.

2.4. Casting of the Target Alloy and Powder Atomization

Based on the measurements of the melting intervals described in Section 2.3, the target alloy that showed the most promising melting ranges for the intended process was selected. Subsequently, a sufficient amount of material (46 kg) for the cylinder-shaped electrodes for the EIGA process was produced by gravity die-casting from the target alloy using a resistance-heated tilting crucible furnace. Aluminum ingots (99.5% purity) and Al-Si master alloy pieces were heated to 680–720 °C and held for approximately 50 min. Then, pure Zn pieces (> 99% purity) were added and a melt treatment with argon was performed twice, using an impeller to minimize the hydrogen content inside the melt. The melt was then poured into a cylindrical die made of mild steel, which was coated with boron-nitride. After machining of the surface, the cast billet had a diameter of 150 mm and a length of 580 mm. Four electrodes (Ø 60 mm each) were machined out of the cast billet.

Atomization of these target alloy electrodes was carried out at TLS (Eckart TLS GmbH, Bitterfeld-Wolfen, Germany) using the EIGA process. The alloy powders were then fractionated using a versus 1000 sieve shaker and a sieve tower (Retsch GmbH, Haan, Germany), which was equipped with stainless steel analytical sieves of mesh sizes 710, 180, 90, 63 and 45 µm.

2.5. Characterization of the Alloys

The chemical compositions of the alloys produced in the laboratory scale as well as the die-cast alloy for EIGA were determined primarily by means of spark spectrometry using a SPECTROMAXx device (Spectro Analytical Instruments GmbH, Kleve, Germany). With the measuring method available on the spark spectrometer, zinc contents up to 12 wt.% could be measured with high accuracy. However, the zinc content in the eight alloys produced is as high as 28 at.% (cf. Table 1), which equals more than 35 wt.% zinc; therefore, the measurements from the spark spectrometer had to be supplemented by analyses with energy dispersive X-ray spectroscopy (EDS). To this end, the EDS-detector (Bruker Corporation, Billerica, MA, USA) of a Supra 55 VP field-emission scanning electron microscope (FE-SEM) (Carl Zeiss AG, Oberkochen, Germany) was used to determine the high zinc fractions in the experimental alloys. In addition, EDS analyses were carried out on the powdered alloy embedded into conductive resin.

2.6. Design of Experiments for the Characterization of the Foaming Behavior

Based on the powder metallurgical process described by Yu et al. [23] and Lehmhus [24], a method for the preparation of foamable semi-finished products for the hybrid billet was developed. In this approach, the alloy powder was mixed with a blowing agent powder and then compacted axially. The influences of the main parameters particle size, blowing agent content, temperature and foaming duration on the expansion behavior of the alloy were investigated using a design of experiments (DoE) approach, see Table 2. There were five different levels obtained for each of the four mentioned factors (particle size, blowing agent, temperature, foaming duration) [25,26]. The resulting foam qualities were evaluated by means of the following qualitative and quantitative properties:

- homogeneity of the pore distribution relative to their position inside the sample;
- distribution of the occurring pore sizes and wall thicknesses;
- overall volume percentage of the porosity of the foam.

The temperature-time regimes of the foaming tests were then used to established extrusion parameters for the EN AW-6082 alloy, which features a microstructure that is sensitive to the actual processing parameters [16,27].

Preliminary tests showed that a temperature of at least 550 °C is required for foaming a sample, which is realized best by the controlled heat treatment subsequent to extrusion. Thus, temperatures between 550 and 650 °C were selected for the foaming experiments. Furthermore, foaming durations between 1 and 7.5 min were selected. According to the literature, blowing agent contents between 0.2 and 1.5 wt.% were used [2,3]. Non-heat-treated titanium dihydride (TiH₂, powder, p.a., PyroPowders) was used as the blowing

agent. The particle size distribution D90 was 45 μm (90% of the particles have a size <45 μm) as quoted by the manufacturer. According to Hipke et al., the release of hydrogen starts just above 400 $^{\circ}\text{C}$ and shows a maximum of the released gas volume at 524 $^{\circ}\text{C}$. The release rate decreases subsequently until 550 $^{\circ}\text{C}$, then increases and reaches a global maximum at 626 $^{\circ}\text{C}$ [3]. The test temperatures of the DoE were based on these findings. The statistical program minitab version 2019 was used in order to support the evaluation of the DoE (Table 2) for the foaming experiments.

Table 2. DoE for the foaming experiments.

Sample	Particle Size, μm	Blowing Agent Content, wt. %	Temperature, $^{\circ}\text{C}$	Foaming Duration, Min
1	<45	0.2	550	1.0
2	<45	0.5	575	2.0
3	<45	0.7	600	3.0
4	<45	1.0	625	5.0
5	<45	1.5	650	7.5
6	45–63	0.2	575	3.0
7	45–63	0.5	600	5.0
8	45–63	0.7	625	7.5
9	45–63	1.0	650	1.0
10	45–63	1.5	550	2.0
11	63–90	0.2	600	7.5
12	63–90	0.5	625	1.0
13	63–90	0.7	650	2.0
14	63–90	1.0	550	3.0
15	63–90	1.5	575	5.0
16	90–180	0.2	625	2.0
17	90–180	0.5	650	3.0
18	90–180	0.7	550	5.0
19	90–180	1.0	575	7.5
20	90–180	1.5	600	1.0
21	<45 + >90	0.2	650	5.0
22	<45 + >90	0.5	550	7.5
23	<45 + >90	0.7	575	1.0
24	<45 + >90	1.0	600	2.0
25	<45 + >90	1.5	625	3.0

The powder mixtures to be foamed were mixed in a Turbula tumbling mixer (Willy A. Bachofen AG, Muttens, Switzerland) and processed into pellets using a 0.8 MN hydraulic press (Matra, Hainburg, Germany) with a custom-made die setup. After compaction, the pellets had a weight of approx. 10 g, a diameter of 35 mm and a height of approx. 3 mm. The maximum ram force of approx. 790 kN resulted in a stress of approx. 208 MPa, which acted on the specimen for 15 min. The temperature of the die was 300 $^{\circ}\text{C}$.

For the foaming experiments, shown in Figure 5, a foamable sample and a reference sample were positioned in the center between two infrared (IR) heat emitters on a 1-millimeter thick steel sheet, which itself lay on a steel mesh. Three thermocouples were inserted into the reference sample. Two thermocouples were used to control each of the upper and lower radiators individually. The third thermocouple was used for temperature recording in the reference sample.

To avoid melting the reference sample, it was made of pure aluminum instead of the low-melting aluminum alloy developed in this study. Due to the different heat capacities and conductivities of the foamable samples and the reference sample, it can be assumed that the samples and the reference show deviating heating behavior. The heating behavior of the reference sample was, therefore, determined separately at the beginning and programmed into the process control. The desired target temperature of the reference sample was maintained with a range of ± 0.5 $^{\circ}\text{C}$ after a short stabilization phase of approx. 30 s; therefore, the target temperature was reproducibly set in the foamable sample. Despite

ensuring reproducible boundary conditions for the heating process, the foaming process of the individual samples shows an unavoidable stochastic component. The compacted powder samples were heated according to the temperature curve shown in Figure 6. After thermal stabilization of the system and a holding time of 60 min at 450 °C, the samples were heated up to the respective desired foaming temperature (see Table 2). A heating rate of 50 °C/min was used. Upon reaching the intended heating duration, the IR emitters were switched off and cooling was carried out in ambient air.

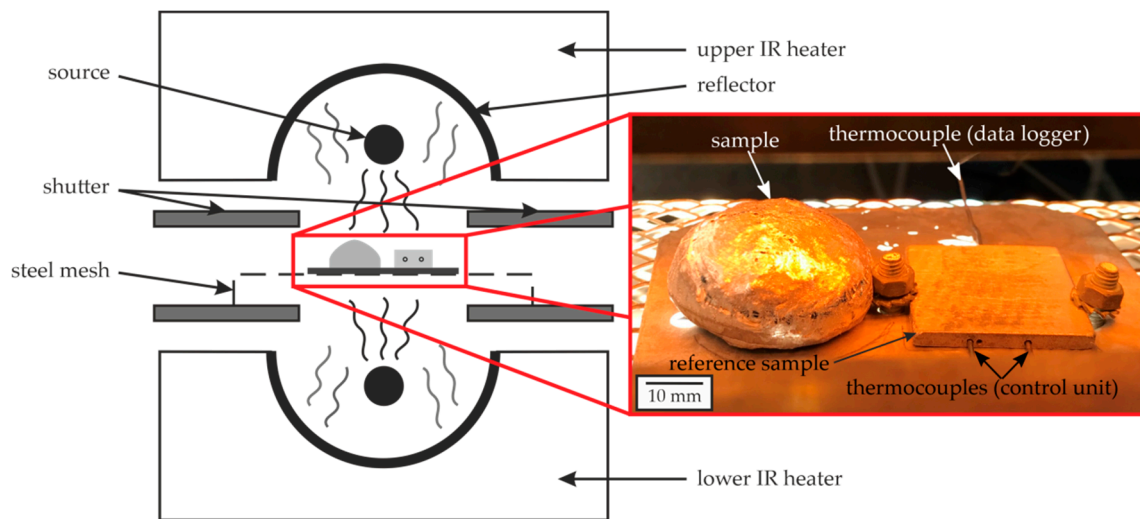


Figure 5. Schematic representation of the heating device used for the foaming experiments and an actual image of a foam sample next to the reference sample used for temperature measurement.

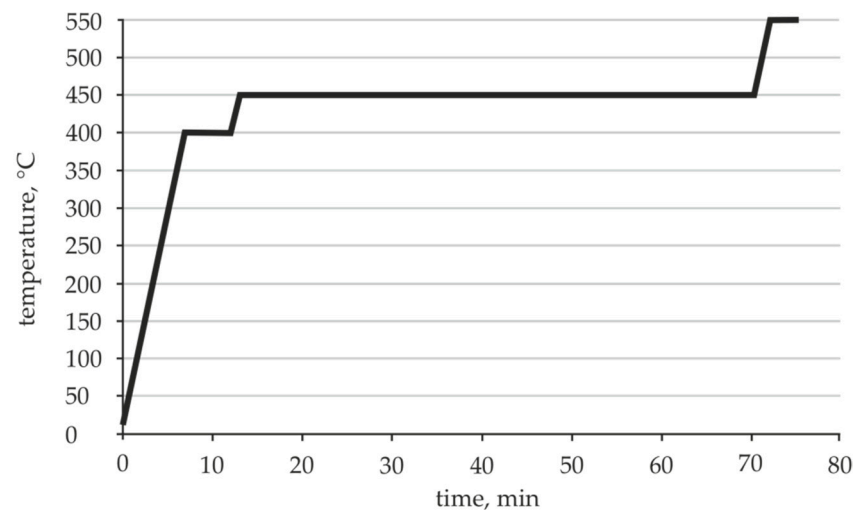


Figure 6. Graphical representation of the temperature-time curve for an exemplary heat treatment of a foamable sample at 550 °C for 3 min.

2.7. XRM Measurements of the Foamed Samples

The porosities of the heat-treated samples depending on the DoE factors (Table 2), were analyzed by means of X-ray microscopy (XRM) using an Xradia 520 Versa (Carl Zeiss AG, Oberkochen, Germany). An acceleration voltage of 90 kV and a power of 6 W were used. The exposure time for each measurement was between 3 and 10 s, depending on the density of the sample. The 3D models of the samples were evaluated with the image-processing software Dragonfly 3 (Object Research Systems Inc., Montreal, QC, Canada). For the determination of porosity, the largest possible cylindrical volume of interest (VOI) from

the center of the sample was considered, and its sample volume V_Z was determined with the image-processing program. The different gray values were then used to distinguish between pores and material and to determine the material volume V_M . Finally, the pore volume, V_P , was determined as the difference between both volumes as follows:

$$V_P = V_Z - V_M \quad (1)$$

With the volume, V_Z , the porosity, P , was determined as follows:

$$P = V_P / V_Z \quad (2)$$

In the present study, the determined values for the porosity of the actual cylinder volume were considered to be representative for the porosity of the whole sample.

3. Results

3.1. Die Temperatures in the Extrusion Processes and Melting Interval of the Novel Al-Zn-Si Alloys

The extrusion experiments on EN AW-6082 showed that for an extrusion ratio of 13:1, a temperature of 485 °C resulted inside the tool near the forming zone. For an extrusion ratio of 22:1, a temperature of 495 °C was measured. Compared with the initial billet temperature, this corresponds to a 35 and 45 °C temperature increase, respectively, due to forming. This temperature increase can be exploited to start the foaming process, if the temperatures reached in the forming zone during extrusion are above the solidus temperature of the foamable aluminum-based alloy. Still, to allow for the complete foam-filling of the hollow profile, a heat treatment subsequent to extrusion will be necessary, which means that the melting interval of the foamable alloy has to be significantly lower than the melting interval of the 6082 alloy.

The chemical compositions shown in Table 3 were determined using spark spectrometry as well as EDS on the samples manufactured according to Section 2.3. The results show that the targeted alloy compositions could be realized with a maximum deviation of 0.3 at.% in the casting process. The theoretical density was calculated according to Equation (3) with the assumption that the materials do not chemically react with each other or do not form an alloy. In the equation, ρ_n is the density for Al, Zn and Si, and m_n is the weight percent of each element in alloy no. 1–8. This equation was used to roughly calculate the filling weight of the ingot molds for the casting tests.

$$\rho = \frac{1}{\sum_{n=0}^k \frac{1}{\rho_n} * m_n} \quad (3)$$

Table 3. Actual chemical compositions of the low-melting aluminum alloys.

Alloy	Designation	Zn Content in at. %	Si Content in at. %	Al Content in at. %	Theoretical Density in g/cm ³
1	AlZn22Si6	21.5	6.0	balance	3.55
2	AlZn22Si6.5	21.7	6.5	balance	3.56
3	AlZn22Si7.5	22.3	7.5	balance	3.58
4	AlZn22Si8	21.8	7.9	balance	3.55
5	AlZn23.5Si8.5	23.6	8.3	balance	3.63
6	AlZn25Si7	25.1	7.1	balance	3.70
7	AlZn26Si6.5	26.0	6.3	balance	3.74
8	AlZn28Si5	28.2	5.2	balance	3.84

The results of the DSC measurements for the analysis of the eight alloys' melting intervals are shown in Figure 7. Alloys one to three have a zinc content of approx. 22 at.% and feature increasing amounts of silicon from alloy one to three. With an increasing

content of silicon, the melting interval is shifted to higher temperatures. Alloy four also has 22 at.% of zinc and a silicon content that is 0.4 at.% higher than that in alloy three. However, this alloy did not show a shift of the melting interval toward higher temperatures. For alloys five to eight, which have a composition along the eutectic channel with an increasing zinc content and decreasing silicon content, the melting interval became slightly wider, with the exception of alloy eight that showed the lowest solidus and liquidus temperatures overall.

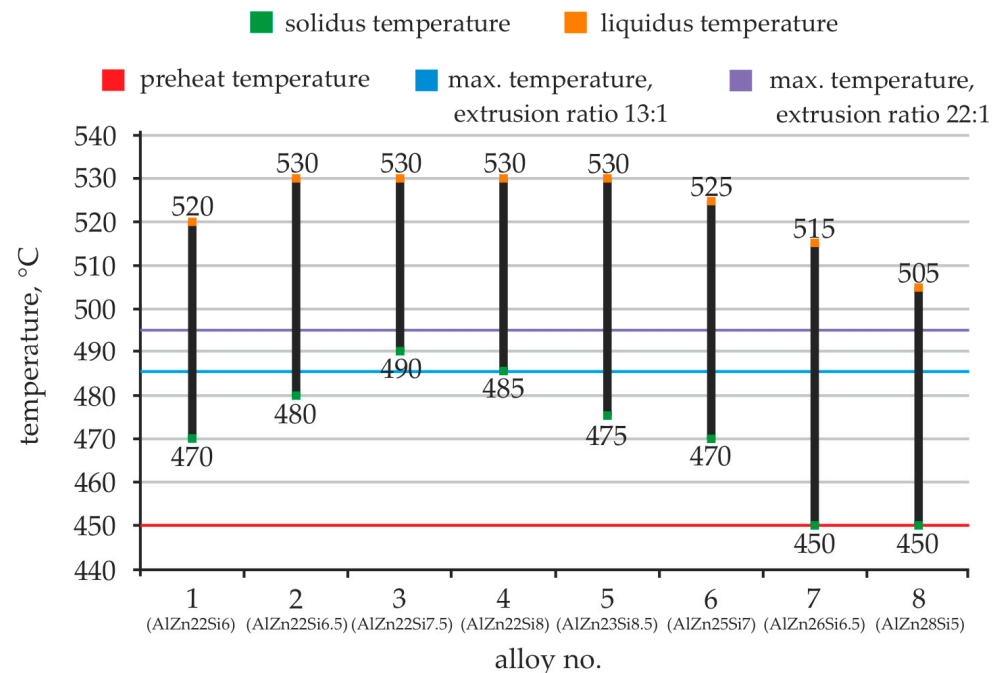


Figure 7. Determined melting intervals of the Al-Zn-Si alloys 1 to 8.

The measured liquidus temperatures of alloys no. one to eight are all well below the melting interval of alloy 6082, which was determined by Birol et al. [28] to be 603–649 °C. For the present approach, the foamable alloy has to meet the following two requirements: (i) the liquidus temperature should be as low as possible, and (ii) the solidus temperature has to be above the ingot preheating temperature of 450 °C. From Figure 1, alloy one (AlZn22Si6) is best suited as it combines a low liquidus temperature with a solidus temperature of 470 °C, which is still above the preheating temperature of the extrusion billet of 450 °C. Its narrow melting interval is considered a positive property for the subsequent foaming process, as the viscosity of the melt above the liquidus temperature is assumed to be lower than in the melting interval. The expansion of the gas released by the blowing agent in the foaming process step is, therefore, facilitated. In addition, alloy one features a slightly lower fraction of heavier alloying elements compared to alloy six, which is beneficial with respect to the application in lightweight construction. Thus, alloy one was selected for the further investigations.

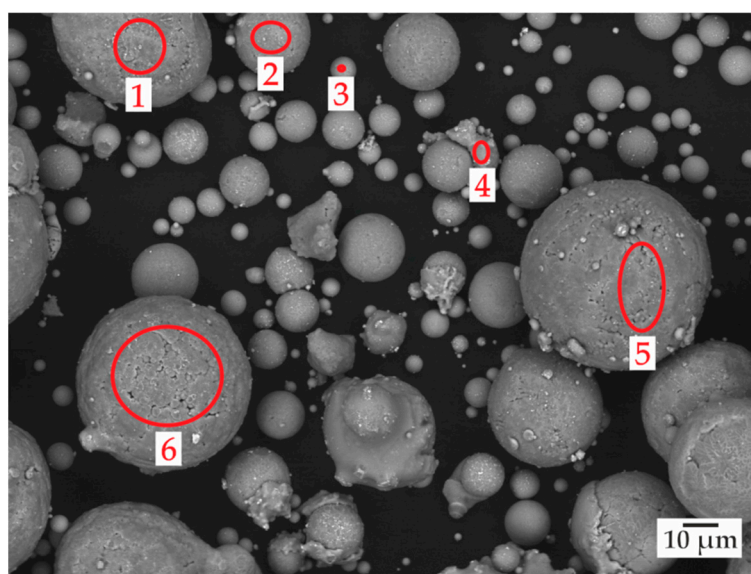
For this purpose, a casting of approx. 47 kg of alloy one was made. To analyze the chemical composition of the cast billet, spark spectrometry was used (Table 4). For these measurements, one sample each from the top area and the bottom area of the cast billet was analyzed. In this case, the determination of all the element fractions of the composition including zinc was conducted on the spark spectrometer by extrapolating the calibration curve slightly outside the calibrated range toward higher zinc contents.

Table 4. Chemical composition of the cast AlZn22Si6-billet in at.%; SD: standard deviation.

	Zn Content	SD	Si Content	SD	Al Content
Top area of the cast billet	20.1	±1.6	6.3	±1.2	balance
Bottom area of the cast billet	23.1	±2.0	5.4	±0.7	balance
Average	21.6		5.8		balance

3.2. Characterization of the Powder Particles Produced via EIGA

Alloy one was atomized into particles using the EIGA process. Figure 8 shows a representative SEM image of AlZn22Si6 particles, which are seen to be predominantly spherical. The chemical composition of the powder particles was determined using EDS analysis in the SEM (Table 5).

**Figure 8.** AlZn22Si6 powder with marked measuring areas 1 to 6 (EDS results in Table 5).**Table 5.** Results of the EDS measurement for the areas 1 to 6 from Figure 8 in at.%; the regions of interest (ROI) are marked in Figure 8; the relative error of the individual measurements is less than 5%.

Element	ROI 1	ROI 2	ROI 3	ROI 4	ROI 5	ROI 6
Al	68.2	65.7	73.3	67.3	70.0	69.5
Zn	25.5	25.3	17.6	26.1	22.2	24.6
Si	6.3	9.0	9.1	6.6	7.8	5.9

The results of the ROI 1–6 measurements show a variation of the alloying elements between the individual particles greater than the measurement error. Although the EDX measurements of the individual powder particles show deviations from the intended alloy composition of alloy no. one, it can be assumed that a uniform distribution of the alloying elements in the volume is achieved by the thorough mixing of the powder particles prior to the preparation of the foamable samples.

3.3. Porosity of the Foamed Alloy

The porosities inside the samples produced in the foaming experiments performed with alloy one were characterized using XRM. The results of the 25 samples, which differed in the combination of particle size, blowing agent content and temperature-time regime

during foaming, are given in Table 6. For the structuring of the results, the following three sample categories were defined depending on the obtained foam porosity:

- Category I: Porosity < 49%
- Category II: Porosity from 49% to 69%
- Category III: Porosity > 69%

Table 6. Porosity of the foamed samples described in Table 2 as determined using XRM.

Sample	1	2	3	4	5	6	7	8	9	10
Porosity <i>P</i> , %	15.6 (I)	26.8 (I)	65.4 (II)	76.0 (III)	80.8 (III)	49.9 (II)	63.4 (II)	78.3 (III)	74.1 (III)	4.8 (I)
Sample	11	12	13	14	15	16	17	18	19	20
Porosity <i>P</i> , %	69.6 (III)	56.0 (II)	79.4 (III)	24.1 (I)	54.1 (II)	61.4 (II)	80.9 (III)	24.6 (I)	56.2 (II)	64.5 (II)
Sample	21	22	23	24	25					
Porosity <i>P</i> , %	76.7 (III)	4.9 (I)	6.5 (I)	47.8 (I)	81.0 (III)					

In Table 6, the classification in the respective category is shown in brackets below the determined value.

Figure 9 shows an example from a sample with little expansion (category I), in two different sectional planes. Many small pores in the micrometer range and a few larger pores that are unevenly distributed characterize the sample. Overall, pore evolution was still in an early state and the height of the foam sample had hardly changed compared to the precursor. Locally, some large pores reached a length of up to approx. 4 mm.

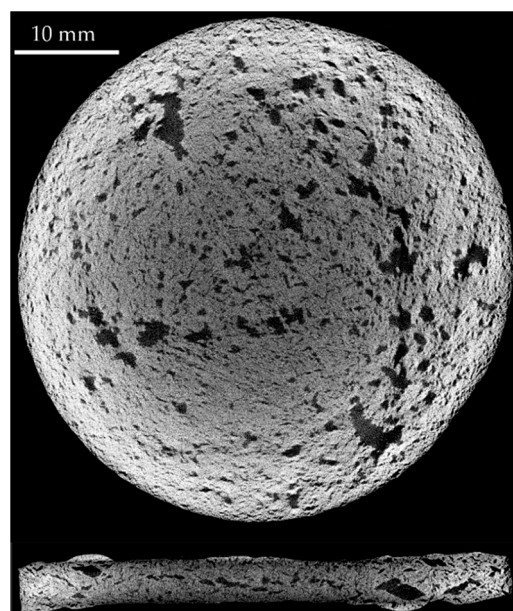


Figure 9. XRM sectional images of sample no. 1 (sample category I): foaming temperature, 550 °C; foaming time, 1 min; 0.2 wt.% TiH_2 .

Sample no. 12 is shown as a typical example for sample category II (Figure 10). Compared to the previous sample, the pore structure of this foam is significantly more mature, and the pores are characterized by a homogenous distribution over the entire sample volume, with most pores having a size between 0.1 and 0.5 mm. Some larger pores with sizes up to 5 mm were also present.

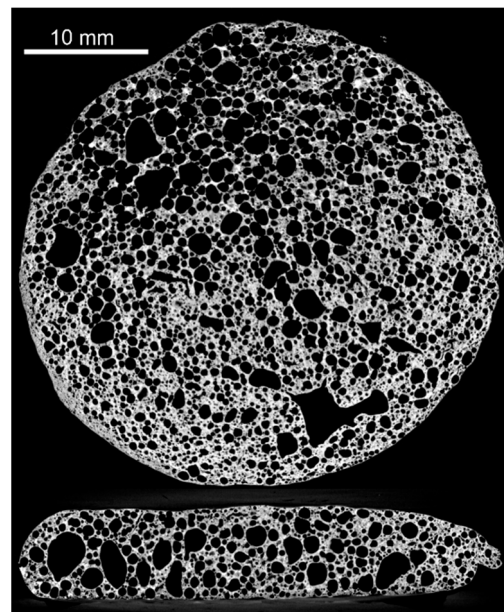


Figure 10. XRM sectional images of sample no. 12 (sample category II): foaming temperature, 625 °C; foaming time, 1 min; 0.5 wt.% TiH₂.

In the following figures, the XRM sectional images of four of the eight samples of category III are shown to demonstrate the differences between each of them regarding pore formation. The sectional images in Figure 11 show foam samples no. eight and no. nine. The structures of both foams are similar, even though the underlying parameters, such as the foaming duration, differ significantly. The maximum pore size was about 8 mm in both cases and most of the pores had a size between 0.5 and 3 mm. The thickness of the cell wall varied between tens of micrometers and about 500 μ m.

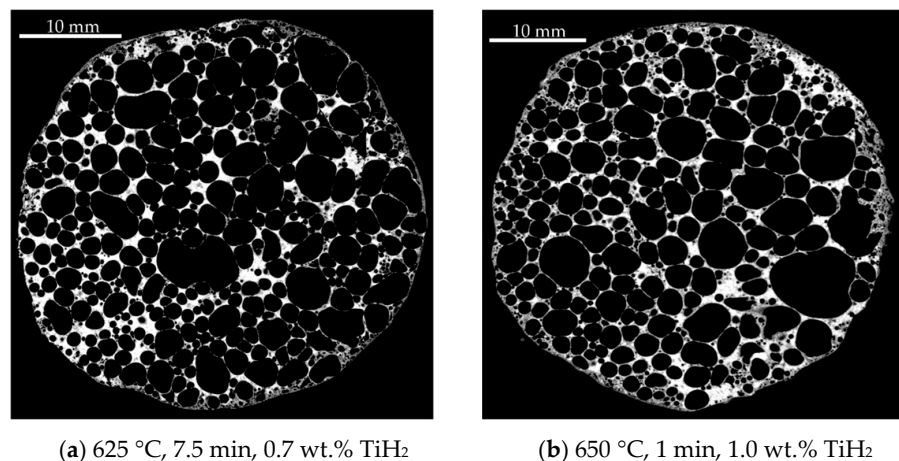


Figure 11. XRM sectional images of sample (a) no. 8 with foaming temperature of 625 °C, foaming duration of 7.5 min, 0.7 wt.% TiH₂ and (b) no. 9 with foaming temperature of 650 °C, foaming duration of 1 min, 1.0 wt.% TiH₂.

Figure 12 shows two cross-sectional views of specimens whose manufacturing parameters differ less than those of the specimens shown in Figure 11. Figure 12a shows foam no. 17, the structure of which is comparatively irregular and is dominated by large pores with a diameter of up to 10 mm. Yet, there are also pores smaller than about 0.1 mm. The latter are predominantly located along the outer wall of the specimen. In contrast, foam no. 21 exhibited the most homogeneous foam structure of all the foamed samples examined

(Figure 12b). The pore size varied between approx. 1 and 3 mm, which also corresponds to the maximum pore size. In the cell walls, hardly any small pores could be detected.

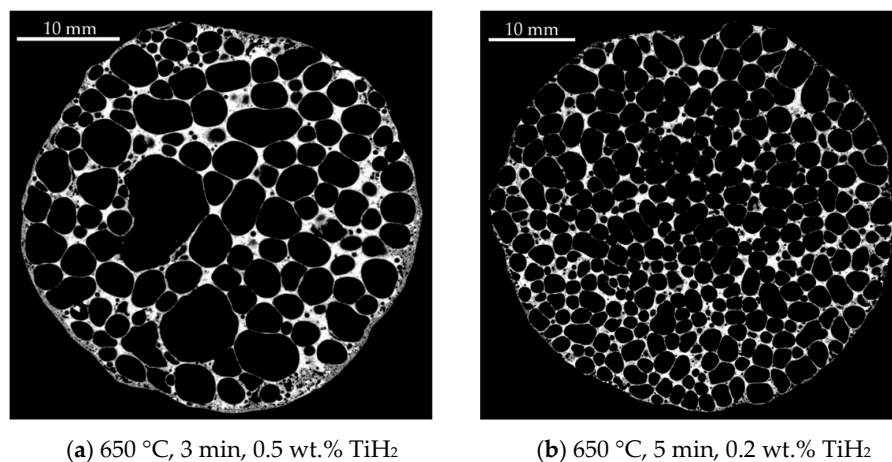


Figure 12. XRM sectional images of sample (a) no. 17 with foaming temperature of 650 °C, foaming duration of 3 min, 0.5 wt.% TiH₂ and (b) no. 21 with foaming temperature of 650 °C, foaming duration of 5 min, 0.2 wt.% TiH₂.

In the samples foamed at high temperatures or with a higher blowing agent content, cracks in the cell walls between pores could be observed in the XRM images, cf. Figure 13. This phenomenon is also referred to in the literature as “wall rupture events” [29]. The extent of the observed phenomenon varies between the foam samples, and the samples with low blowing agent content, such as sample no. 11 (Figure 14), show almost no wall rupture events.

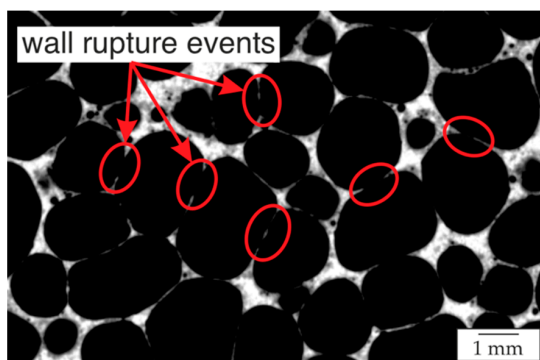


Figure 13. Section of the XRM image of sample no. 21 with foaming temperature of 650 °C, foaming duration of 5 min, 0.2 wt.% TiH₂ with wall rupture events marked in red.

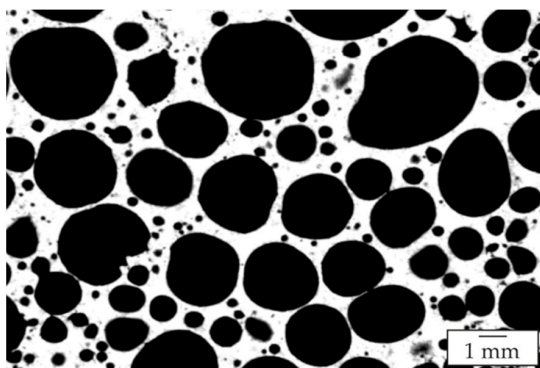


Figure 14. Section from the XRM image of sample no. 11 with foaming temperature of 600 °C, foaming duration of 7.5 min, 0.2 wt.% TiH₂ showing intact cell walls.

3.4. Foam Quality

The influence of the “particle size”, “blowing agent content”, “foaming temperature” and “foaming duration” factors on the quality characteristics of porosity and the homogeneity of the pores (size distribution and distribution of the pores over the sample cross-section) was determined in the DoE evaluation. The higher the mean value of the quality characteristic varies within a factor range, the higher the influence or effect of the corresponding factor on it. As shown in Figure 15, the temperature has the most significant influence on the porosity. It is also obvious that the particle size as well as the blowing agent content have less influence on the quality characteristic of porosity than the foaming duration. For the “particle size” factor, it has been shown that mixing small and large particles has no positive effect on the achievable porosity; the opposite is in fact the case, as the lowest average porosity was observed. The “blowing agent content” factor did not show any significant influence on the porosity when varying the contents from 0.2 to 1.5 wt.%. In the case of the “temperature” factor, it was found that the positive influence on porosity becomes greater with an increasing temperature up to 650 °C. The trend suggests that higher temperatures, not investigated in this study, may lead to an even higher porosity of the foam specimens. After a 2-minute “foaming duration”, a leap in porosity is detected. Thus, higher porosities were observed at values of 3 to 7.5 min, compared to durations of 1 and 2 min.

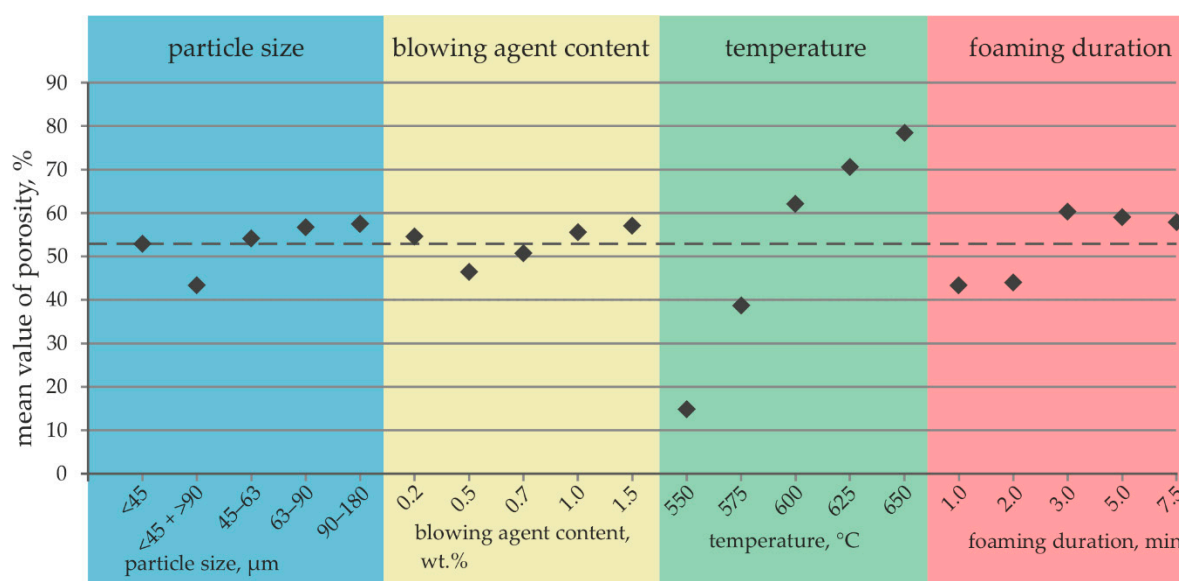


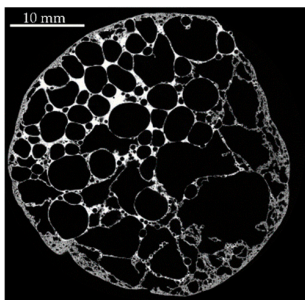
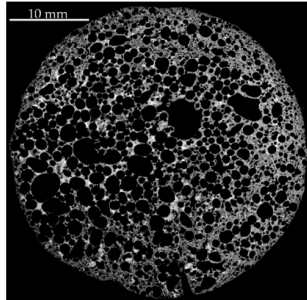
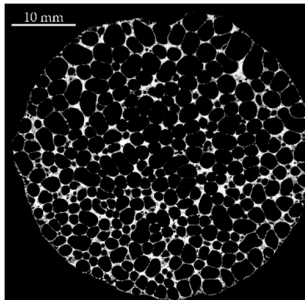
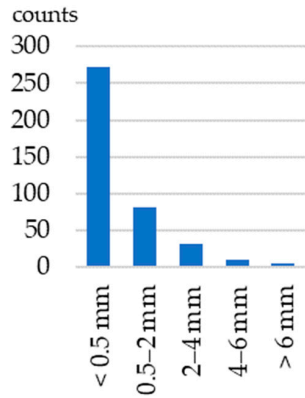
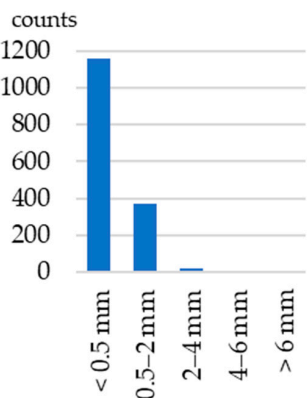
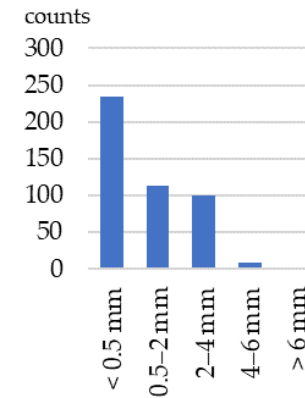
Figure 15. DoE evaluation of the effects of the investigated factors on the quality characteristic porosity.

In addition to the porosity, it was investigated how uniformly the metal foam was formed. For the DoE evaluation of the quality characteristic of foam homogeneity, three homogeneity levels were defined, as follows:

- Homogeneity level 1: The foam has an overall non-uniform foam structure
- Homogeneity level 2: The foam has a more homogeneous cell structure overall, but contains significantly enlarged pores in some areas and a large number of very small pores in other areas
- Homogeneity level 3: The foam has an almost equal pore size and distribution over the entire sample.

This resulted in the following classification of the samples into the three homogeneity levels (see Table 7). In order to describe the quantitative distribution of the pore area in the two-dimensional cross-sectional images shown, the equivalent circular diameter of the pore areas in the image processing software Stream (Olympus Europa SE & Co. KG, Hamburg, Germany) was determined.

Table 7. Classification of the foam samples into the three homogeneity levels; note the different scales of the y-axis.

Homogeneity Level	1	2	3																																				
Representative XRM image																																							
Distribution of equivalent circular diameters of pore areas in the sectional view shown	 <table><tr><th>Pore Size Range (mm)</th><th>Counts (approx.)</th></tr><tr><td>< 0.5</td><td>280</td></tr><tr><td>0.5–2</td><td>80</td></tr><tr><td>2–4</td><td>30</td></tr><tr><td>4–6</td><td>10</td></tr><tr><td>> 6</td><td>5</td></tr></table>	Pore Size Range (mm)	Counts (approx.)	< 0.5	280	0.5–2	80	2–4	30	4–6	10	> 6	5	 <table><tr><th>Pore Size Range (mm)</th><th>Counts (approx.)</th></tr><tr><td>< 0.5</td><td>1100</td></tr><tr><td>0.5–2</td><td>350</td></tr><tr><td>2–4</td><td>20</td></tr><tr><td>4–6</td><td>5</td></tr><tr><td>> 6</td><td>2</td></tr></table>	Pore Size Range (mm)	Counts (approx.)	< 0.5	1100	0.5–2	350	2–4	20	4–6	5	> 6	2	 <table><tr><th>Pore Size Range (mm)</th><th>Counts (approx.)</th></tr><tr><td>< 0.5</td><td>230</td></tr><tr><td>0.5–2</td><td>110</td></tr><tr><td>2–4</td><td>100</td></tr><tr><td>4–6</td><td>10</td></tr><tr><td>> 6</td><td>5</td></tr></table>	Pore Size Range (mm)	Counts (approx.)	< 0.5	230	0.5–2	110	2–4	100	4–6	10	> 6	5
Pore Size Range (mm)	Counts (approx.)																																						
< 0.5	280																																						
0.5–2	80																																						
2–4	30																																						
4–6	10																																						
> 6	5																																						
Pore Size Range (mm)	Counts (approx.)																																						
< 0.5	1100																																						
0.5–2	350																																						
2–4	20																																						
4–6	5																																						
> 6	2																																						
Pore Size Range (mm)	Counts (approx.)																																						
< 0.5	230																																						
0.5–2	110																																						
2–4	100																																						
4–6	10																																						
> 6	5																																						
Foam samples No.	1, 3, 5 (this image), 10, 13, 14, 15, 16, 17, 18, 20, 22, 23, 24 and 25	2, 4, 6, 7 (this image), 8, 9, 12 and 19	11 and 21 (this image)																																				

The DoE analysis based on the homogeneity levels is shown in Figure 16. The comparison of the four factors shows that the “blowing agent content” factor has the greatest influence on the homogeneity of the pores. Here, low blowing agent contents show a positive and very high contents a negative effect. In the case of the quality characteristic porosity, this factor did not show any great influence (see Figure 15). However, the foams with the highest blowing agent content (no. 5 and no. 25) had the most irregular pore structure and the largest pores. In addition, more “wall rupture events” were found in these samples. The “particle size” factor showed that smaller particles lead to low average homogeneities of the pores, even when mixed with larger particles. A maximum is reached at the average size fraction of 45–63 μm . Comparatively large particles have a negative effect. The influence of the “temperature” factor has a minor effect on the quality characteristic of homogeneity, in contrast to the quality characteristic of porosity, where the factor is dominant. For the “foaming duration” factor, a leap to higher average values with longer durations can be observed, similar to the quality characteristic of porosity (see Figure 15). The leap in the quality characteristic of homogeneity occurs from 3 to 5 min and is, thus, slightly shifted to longer foaming durations.

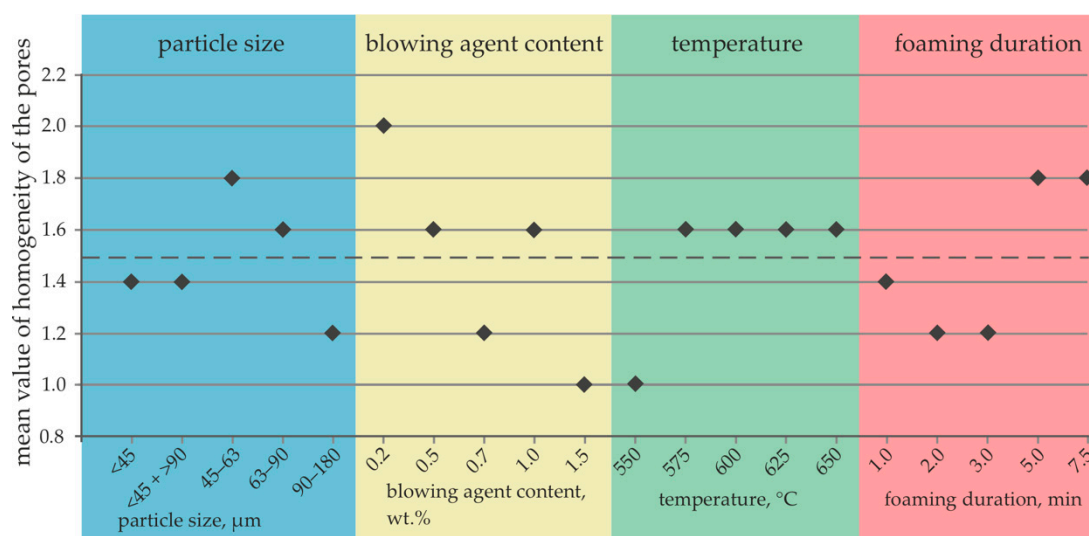


Figure 16. DoE evaluation of the effects of the investigated factors on the quality characteristic of the homogeneity of the pores.

4. Discussion

In the present study, multiple alloys of the Al-Zn-Si system were prepared, whose composition was along the eutectic channel (according to the ternary phase diagram of Suzuki [19]). In all the cases, the addition of Zn and Si shifted the melting interval towards lower temperatures compared to pure aluminum and that of the Al-Si-Mg wrought alloy EN AW-6082. The alloys seven and eight, which had the highest zinc content out of the eight alloys, showed a melting interval with the lowest solidus temperatures of about 450 °C. Since this temperature corresponds to the billet preheating temperature [30,31] of extrusion billets made of EN AW-6082, such a low solidus temperature is not suitable for the planned application of process integrated foaming during extrusion, as the melting and premature foaming of the preheated hybrid billet would occur. Simultaneously, the aggregate state changes greatly reduce the deformation resistance of the Al-Zn-Si alloy and increase the difference between the flow stresses of EN AW-6082 and the foamable alloy, which makes a co-extrusion process more challenging [29]. Alloys with a very high zinc content (>25 at.%) are, therefore, not suitable for the intended process route.

Increasing the Si content while maintaining that of Zn constant (alloys two to four) did not have the desired effect on the melting interval, and the temperature range between solidus and liquidus temperature could not be reduced. With an increasing deviation from a eutectic composition by increasing the content of Si, the melting interval shifted towards higher temperatures. Overall, alloy one, with a melting interval of 470–520 °C, exhibited the most suitable properties for the intended process chain and was, therefore, selected for the foaming experiments. In addition, alloy one exhibits a mass density up to 8.2% lower than alloys 5–8, since it contains less Zn. A lower density of the material results in a lower mass of the later component, which is advantageous for applications in lightweight structures [30].

The results of the foaming experiments showed that the “foaming temperature” factor has the most significant influence on the resulting porosity in the metal foam. These results are in accordance with the observations of Duarte and Banhart [31], despite the differing alloy compositions. They studied the expansion of AlSi7 foam samples at different temperatures between 600 and 800 °C (in 25 °C steps). In the present study, the same blowing agent, TiH₂, was used for the foaming tests of the lower-melting AlZnSi alloy, and the range of blowing agent content also overlapped.

A sudden increase in the influence of the “foaming duration” factor on the volume increase in the foam specimens was observed between 2 and 3 min. This can be explained by a complete melting of the material, which accelerates volume expansion. This was

referred to by Hipke et al. [3] as phase three of the stages of the foaming process. This four-phase model (1. unexpanded precursor, 2. preheating of the pressed metal mixture, 3. fully heated and expansion, 4. partial collapse of the foam after the maximum expansion) can also explain another result of the study presented here. With increasing foaming durations of 5 and 7.5 min, a decrease in porosity was observed due to an over-aging of the foam. The unstable foam thus partially collapsed. This can be explained by foam drainage and the coarsening of gas bubbles due to gas diffusion from one pore to another [3]. The observed increased occurrence of “wall rupture events” in the foam samples with higher blowing agent contents or higher foaming temperatures also possibly led to mechanical weakening. This is assumed because larger pressure differences due to the increased blowing agent content and more melt fractions due to the higher process temperatures presumably lead to “bubble flow” and “drainage”, and thus to a mechanical weakening of the cell walls as proposed by Banhart [32] and Helfen et al. [33]. Due to the partial wall rupture between the pores, the propellant gas could leak relatively easily from one pore into an adjacent cell. This then leads to the formation of large-volume individual pores that deviate significantly from the average pore volume.

The evaluation of the results that was supported by the DoE method revealed that the blowing agent content has only a minor influence on the porosity of the foams, but it had the most significant influence on the homogeneity among the factors investigated in this study. Figure 16 shows that the homogeneity decreases with an increasing blowing agent content. It can be assumed that the increased amount of released hydrogen promotes the coalescence of pores and coarsening of the gas bubbles as described by Hipke et al. [3] and Körner [29]. These effects lead to a reduction in the number of pores in the sample, but an increase in the volume of the pores created. Thus, homogeneously distributed small pores are no longer found, and the samples were classified in homogeneity level one or two. In addition to the effects mentioned, drainage caused by gravity was also found. In this case, melt flowed from the upper part of the sample to the lower part during the foaming process. This melt drainage caused a thinning of the cell walls in the upper area, and thus supports the coalescence of pores and the pore coarsening in this upper part of the sample.

5. Conclusions and Outlook

In the present study, low-melting aluminum alloys with different zinc and silicon contents were investigated to establish an essential step towards a process-integrated foaming of extruded profiles. The present results led to the following conclusions:

- With the composition AlZn22Si6, a promising alloy with a melting range of 470–520 °C was developed for a process-integrated foaming during co-extrusion.
- In standalone foaming experiments, it was observed that the temperature selected for foaming has the greatest influence on the porosity of the metal foam made of the developed AlZnSi alloy. The further parameters, time, particle size and blowing agent content, are less critical with respect to the evolution of the porosity.
- The homogeneity of the pore structure was significantly influenced by the blowing agent content. The foaming temperature parameter had hardly any influence on the homogeneity of the pore distribution over the sample and volume size.
- Using particles of alloy one with a particle size <45 and >90 µm, a blowing agent content of 1.5 wt.%, a foaming temperature of 625 °C and a foaming duration of 3 min, a homogenous metal foam with a high porosity of 81% was successfully produced.

Work is underway to realize the complete process chain for the production of a foamed hybrid profile with the developed foamable alloy.

Author Contributions: Conceptualization, H.J.M. and C.K.; methodology, F.P.S.; investigation, F.P.S.; writing—original draft preparation, F.P.S.; writing—review and editing, H.J.M., C.K. and S.E.T.; visualization, F.P.S. and S.E.T.; supervision, H.J.M. and C.K.; project administration, H.J.M. and C.K.; funding acquisition, H.J.M. and C.K. All authors have read and agreed to the published version of the manuscript.

Funding: This research was funded by the German Research Foundation (DFG) through the project “Aluminium alloys with controlled melting ranges for process-integrated foaming during extrusion”, grant number 324394568. The publication of this article was funded by the Open Access Fund of the Leibniz Universität Hannover.

Institutional Review Board Statement: Not applicable.

Informed Consent Statement: Not applicable.

Data Availability Statement: The data presented in this study are available on request from the corresponding author. The data are not publicly available due to ongoing research.

Conflicts of Interest: The authors declare no conflict of interest.

References

1. Ashby, M.F. *Metal Foams: A Design Guide*; Butterworth-Heinemann: Boston, MA, USA, 2000; ISBN 0-7506-7219-6.
2. Banhart, J. Manufacture, characterisation and application of cellular metals and metal foams. *Prog. Mater. Sci.* **2001**, *46*, 559–632. [CrossRef]
3. Hipke, T.; Lange, G.; Poss, R. *Taschenbuch für Aluminiumschäume*, 1st ed.; Aluminium-Verl.: Düsseldorf, Germany, 2007; ISBN 978-3-87017-285-5.
4. Banhart, J. Light-metal foams-history of innovation and technological challenges. *Adv. Eng. Mater.* **2013**, *15*, 82–111. [CrossRef]
5. Banhart, J. 4.14 Production of Metal Foams. In *Comprehensive Composite Materials II*; Elsevier: Amsterdam, The Netherlands, 2018; pp. 347–363.
6. Zhou, W.; Yu, J.; Lu, X.; Lin, J.; Dean, T.A. A comparative study on deformation mechanisms, microstructures and mechanical properties of wide thin-ribbed sections formed by sideways and forward extrusion. *Int. J. Mach. Tools Manuf.* **2021**, *168*, 103771. [CrossRef]
7. Zhou, W.; Yu, J.; Lin, J.; Dean, T.A. Effects of die land length and geometry on curvature and effective strain of profiles produced by a novel sideways extrusion process. *J. Mater. Process. Technol.* **2020**, *282*, 116682. [CrossRef]
8. Duarte, I.; Vesenjaj, M.; Krstulović-Opara, L.; Anžel, I.; Ferreira, J. Manufacturing and bending behaviour of in situ foam-filled aluminium alloy tubes. *Mater. Des.* **2015**, *66*, 532–544. [CrossRef]
9. Duarte, I.; Vesenjaj, M.; Krstulović-Opara, L. Dynamic and quasi-static bending behaviour of thin-walled aluminium tubes filled with aluminium foam. *Compos. Struct.* **2014**, *109*, 48–56. [CrossRef]
10. Plorin, T.; Bormann, D.; Heidenblut, T.; Bach, F.W. Investigations into Manufacturing Composite Profiles Having Local Magnesium-Foam Reinforcements. *Adv. Mater. Res.* **2010**, *137*, 129–160. [CrossRef]
11. Baumeister, J.; Rausch, G.; Stöbener, K.; Lehmhus, D.; Busse, M. Verbundwerkstoffe mit Aluminiumschaum—Anwendungen im Schienenfahrzeugbau. *Mater. Werkst.* **2007**, *38*, 939–942. [CrossRef]
12. Stöbener, K.; Baumeister, J.; Rausch, G.; Rausch, M. Forming metal foams by simpler methods for cheaper solutions. *Met. Powder Rep.* **2005**, *60*, 12–16. [CrossRef]
13. Duarte, I.; Vesenjaj, M.; Krstulović-Opara, L.; Ren, Z. Compressive performance evaluation of APM (Advanced Pore Morphology) foam filled tubes. *Compos. Struct.* **2015**, *134*, 409–420. [CrossRef]
14. Vesenjaj, M.; Gačnik, F.; Krstulović-Opara, L.; Ren, Z. Mechanical Properties of Advanced Pore Morphology Foam Elements. *Mech. Adv. Mater. Struct.* **2014**, *22*, 359–366. [CrossRef]
15. Bauser, M.; Sauer, G.; Siegert, K. *Strangpressen*, 2nd ed.; Aluminium-Verl.: Düsseldorf, Germany, 2001; ISBN 3-87017-249-5.
16. Nowak, M. Prozessintegrierte Abkühlung mittels Wasser-Luft-Spray-Kühlung beim Strangpressen der Aluminiumlegierungen EN AW-6082 und EN AW-Zugl. Master’s Thesis, Hannover University, Hannover, Germany, 2014.
17. Thürer, S.E.; Peddinghaus, J.; Heimes, N.; Bayram, F.C.; Bal, B.; Uhe, J.; Behrens, B.-A.; Maier, H.J.; Klose, C. Lateral Angular Co-Extrusion: Geometrical and Mechanical Properties of Compound Profiles. *Metals* **2020**, *10*, 1162. [CrossRef]
18. Schaffer, G.; Sercombe, T.; Lumley, R. Liquid phase sintering of aluminium alloys. *Mater. Chem. Phys.* **2001**, *67*, 85–91. [CrossRef]
19. Ostermann, F. *Anwendungstechnologie Aluminium*; Springer: Berlin/Heidelberg, Germany, 2014; ISBN 978-3-662-43806-0.
20. Altenpohl, D. *Aluminium und Aluminiumlegierungen*; Springer: Berlin/Heidelberg, Germany, 1965; ISBN 978-3-662-30245-3.
21. Suzuki, T. *Materials Science International Team, MSIT®. Calculated Liquidus Surface: Datasheet From MSI Eureka in Springer Materials*; MSI, Materials Science International Services GmbH: Stuttgart, Germany, 1993; Available online: https://materials.springer.com/msi/phase-diagram/docs/sm_msi_r_10_014605_01_full_LnkDia0 (accessed on 29 May 2018).
22. Usercom. *Interpreting DSC curves Part 1: Dynamic measurements*; Mettler Toledo GmbH, Ed.; Mettler Toledo GmbH: Schwerzenbach, Switzerland, 2000.
23. Yu, C.-J.; Eifert, H.H.; Banhart, J.; Baumeister, J. Metal foaming by a powder metallurgy method: Production, properties and applications. *Mater. Res. Innov.* **1998**, *2*, 181–188. [CrossRef]
24. Lehmhus, D. Beitrag zur Optimierung der Herstellung und der Materialeigenschaften von Aluminiumschäumen. Zugl. Master’s Thesis, Bremen University, Bremen, Germany, 2007.
25. Dean, A.; Voss, D.; Draguljić, D. *Design and Analysis of Experiments*; Springer International Publishing: Cham, Switzerland, 2017; ISBN 978-3-319-52248-7.

-
26. Siebertz, K.; van Bebber, D.; Hochkirchen, T. *Statistische Versuchsplanung*; Springer: Berlin/Heidelberg, Germany, 2017; ISBN 978-3-662-55742-6.
 27. Mrówka-Nowotnik, G.; Sieniawski, J. Influence of heat treatment on the microstructure and mechanical properties of 6005 and 6082 aluminium alloys. *J. Mater. Process. Technol.* **2005**, *162–163*, 367–372. [[CrossRef](#)]
 28. Birol, Y. Thixoforging experiments with 6082 extrusion feedstock. *J. Alloy. Compd.* **2008**, *455*, 178–185. [[CrossRef](#)]
 29. Körner, C. Foam formation mechanisms in particle suspensions applied to metal foams. *Mater. Sci. Eng. A* **2008**, *495*, 227–235. [[CrossRef](#)]
 30. Hirsch, J. Aluminium in Innovative Light-Weight Car Design. *Mater. Trans.* **2011**, *52*, 818–824. [[CrossRef](#)]
 31. Duarte, I.; Banhart, J. A study of aluminium foam formation—Kinetics and microstructure. *Acta Mater.* **2000**, *48*, 2349–2362. [[CrossRef](#)]
 32. Banhart, J. Metal Foams: Production and Stability. *Adv. Eng. Mater.* **2006**, *8*, 781–794. [[CrossRef](#)]
 33. Helfen, L.; Stanzick, H.; Ohser, J.; Schladitz, K.; Rejmankova-Pernot, P.; Banhart, J.; Baumbach, T. Investigation of the foaming process of metals by synchrotron radiation imaging. In *NDE for Health Monitoring and Diagnostics*; SPIE: Washington, DC, USA, 2003; pp. 254–265.